INTERNATIONAL JOURNAL FOR NUMERICAL METHODS IN ENGINEERING
Int. J. Numer. Meth. Engng 2016; **108**:990–1006
Published online 28 March 2016 in Wiley Online Library (wileyonlinelibrary.com). DOI: 10.1002/nme.5242

Isogeometric analysis of fluid-saturated porous media including flow in the cracks

J. Vignollet[1], S. May[1] and R. de Borst[2,*,†]

[1] *School of Engineering, University of Glasgow, Glasgow G12 8LT, UK*
[2] *Department of Civil and Structural Engineering, University of Sheffield, Sheffield S1 3JD, UK*

SUMMARY

An isogeometric model is developed for the analysis of fluid transport in pre-existing faults or cracks that are embedded in a fluid-saturated deformable porous medium. Flow of the interstitial fluid in the porous medium and fluid transport in the discontinuities are accounted for and are coupled. The modelling of a fluid-saturated porous medium in general requires the interpolation of the displacements of the solid to be one order higher than that of the pressure of the interstitial fluid. Using order elevation and Bézier projection, a consistent procedure has been developed to accomplish this in an isogeometric framework. Particular attention has also been given to the spatial integration along the isogeometric interface element in order to suppress traction oscillations that can arise for certain integration rules when a relatively high dummy stiffness is used in a poromechanical model. © 2016 The Authors. *International Journal for Numerical Methods in Engineering* Published by John Wiley & Sons Ltd.

Received 23 June 2015; Revised 17 February 2016; Accepted 18 February 2016

KEY WORDS: isogeometric analysis; poroelasticity; cracks; interface elements; flow

1. INTRODUCTION

Fracture lies in the heart of many cases of failure in natural and man-made materials. Fracture mechanics, as a scientific discipline in its own right, originated in the early 20th century with the pioneering work of Griffith [1]. Driven by some spectacular disasters in the shipbuilding and aerospace industries, and building on the seminal work of Irwin [2], linear elastic fracture mechanics became an important tool in the analysis of structural integrity. Linear elastic fracture mechanics applies when the dissipative processes remain confined to a region in the vicinity of the crack tip that is small compared with the structural dimensions. When this condition is not met, e.g. when considering cracking in more heterogeneous materials like soils, rocks or many biomaterials, cohesive-zone models are preferred [3, 4]. Also for fluid-saturated porous media, Rice and Simons [5] have provide compelling arguments in favour of the use of cohesive-zone models by analysing shear crack growth. Indeed, stationary or propagating cracks in (partially) saturated porous media occur frequently in a number of important applications. The existence or propagation of such cracks can be undesirable, such as in human tissues, or for the storage of waste in rocks or salt domes, but at other times, cracking can be a pivotal element in an industrial process, for example, hydraulic fracturing in the oil and gas industry. Another important application is the rupture of geological faults, where the change in geometry of a fault can drastically affect local fluid flow as the faults can act as channels in which the fluid can flow freely.

As much as the study of fracture in porous materials has not received much attention until recently, at least compared with studies on solid materials, the theory of fluid flow in deforming porous media has practically been confined to intact materials [6–9]. This holds *a fortiori* for *numerical studies*

*Correspondence to: René de Borst, Department of Civil and Structural Engineering, University of Sheffield, Sheffield S1 3JD, UK.
†E-mail: r.deborst@sheffield.ac.uk

on fracture in porous media. Notable exceptions are References [10] and [11], in which standard interface elements were used enhanced with pressure degrees of freedom, so that fluid flow inside the crack can be modelled, Secchi *et al.* [12], who have used remeshing to track a propagating cohesive crack in a porous medium, thereby extending the seminal work of Boone and Ingraffea [13] on fluid-driven crack propagation in impervious media, and de Borst and co-workers [14–18], who have decoupled the crack propagation path in a (partially) fluid-saturated porous medium from the underlying discretisation by exploiting the partition-of-unity concept of (polynomial) finite element shape functions [19]; see also [20, 21].

A disadvantage of the finite element method is that the stress prediction around the crack tip is usually poor. To a lesser extent, this also applies when the crack tip is enriched using tailor-made functions to capture the stress singularities or high stress gradients that typically occur at the tip, or when smoothing techniques are added. For fluid-saturated porous media, standard finite element methods have the additional disadvantage that the fluid flow, which is obtained as the derivative of the pressure, is discontinuous at element boundaries, causing the local mass balance not to be satisfied unless special degrees of freedom are introduced, e.g. [22]. The underlying cause is the same in both cases. The primary variable (displacement and pressure) is only $\mathcal{C}^0$-continuous across element boundaries, causing jumps in the derived quantities as strains and fluid flow.

A promising solution is the use of isogeometric analysis, originally proposed to obtain a seamless connection between computer-aided design tools and analysis tools, with the aim of bypassing the elaborate and time-consuming meshing phase [23–26]. It has been recognised that non-uniform rational basis splines (NURBS), which are the predominant functions in conventional computer-aided design-packages, are not capable of providing local mesh refinement that is often needed in the analysis phase. To remedy this deficiency, T-splines have been proposed [27, 28]. While T-spline technology is very powerful, T-spline meshes of complicated structures can meet at so-called extraordinary points, where three or more than four patches meet. These extraordinary points normally introduce lines of $\mathcal{C}^0$-continuity, thus locally sacrificing the higher smoothness of isogeometric analysis, e.g. [29]. Nevertheless, for most parts of the structure, a higher-order continuity is obtained, which renders derived quantities like strains or fluid flow in porous media, continuous across element boundaries [30]. Local mass balance is automatically satisfied, and the stress prediction is vastly improved.

Biphasic models, in which the displacements for the solid phase and the pressures for the interstitial fluid are interpolated separately, do not necessarily satisfy the Ladyzhenskaya–Babuška–Brezzi condition, e.g. [31, 32]. To meet this *inf–sup* condition, the displacement field is normally interpolated one order higher than the pressure field, e.g. [33], although this is not a sufficient condition and rigorous proofs that an element meets the *inf–sup* condition can be hard to obtain. Notwithstanding this theoretical argument, such interpolations have met with much success in standard finite element formulations. Whereas the independent interpolation of displacements and pressures is rather straightforward in standard finite elements, this is less so for isogeometric finite element analysis, and we will describe a consistent procedure to achieve this.

We will enrich the isogeometric interface element developed in [34] with mass transport within the crack, in a similar manner as was carried out for finite elements that exploit the partition-of-unity property of polynomial shape functions [15]. We note that, because in the present contribution we are only considering stationary discontinuities, we can exploit isogeometric interface elements. However, as noticed in [34], such interface elements can suffer from traction oscillations. An in-depth analysis has been made in [35] for the purely mechanical case, which will herein be extended to poromechanics.

First, we will recapitulate the momentum and mass balance equations for a cracked, fluid-saturated porous medium. Next, we will describe how, using a p-refinement algorithm for NURBS [36], a consistent mixed formulation can be derived using order elevation, Bézier extraction and Bézier projection. Subsequently, weak forms are derived in a standard manner,including the mass coupling between the local scale and the global scale. The numerical integration of poromechanical interface elements will be considered next and will be illustrated at the hand of the example of flow in the quarter of a torus with a crack. A parametric study of the effect of the inclination of a crack on the flow in a fluid-saturated porous medium concludes the paper.

DOI: 10.1002/nme

2. GOVERNING EQUATIONS

2.1. Basic assumptions

We consider the body Ω shown in Figure 1. For simplicity, we consider a fluid-saturated porous medium, consisting of two constituents, a solid phase S and a fluid phase F, but the extension to more phases, e.g. a gas phase, is fairly straightforward. The fundamental assumption of the theory of porous media is that at each spatial point $\mathbf{x} \in \Omega$, particles of all constituents, in this case only a solid and a fluid phase, so that $\alpha = \{S, F\}$, coexist. Therefore, any elementary volume dv is simultaneously occupied by both phases and is split into partial elementary volumes dv^α. This allows to define the volume fractions:

$$n_\alpha(\mathbf{x}) = \frac{dv_\alpha}{dv}, \qquad \alpha = \{S, F\}, \tag{1}$$

which are subject to the saturation condition: $n_S + n_F = 1$.

The concept of volume fractions allows to bypass the difficulty of modelling the complex internal geometry of the microstructure by smearing the constituent properties to obtain an *effective* homogeneous representation of the constituent properties at the macrolevel. The governing equations of each constituent α, weighed by the volume fractions, must be satisfied simultaneously. These are derived independently and added to obtain the governing equations of the mixture. In the remainder, only the equations that govern the mixture are stated; see e.g. [8, 14, 37] for details regarding the derivation of the governing equations. The assumption that the strains remain small is adopted throughout this paper, but the extension of a fluid-saturated medium to include large strains is not too complicated [18].

The body Ω is crossed by an interface Γ_d, splitting the domain Ω into two subdomains Ω^+ and Ω^-, respectively, such that $\Omega = \Omega^+ \cup \Omega^-$. This interface can be either closed or open. The interface Γ_d is equipped with a local coordinate system $(\mathbf{n}_{\Gamma_d}, \mathbf{s}_{\Gamma_d}, \mathbf{t}_{\Gamma_d})$, where $\mathbf{n}_{\Gamma_d}$ is the vector normal to the interface, and $\mathbf{s}_{\Gamma_d}$ and $\mathbf{t}_{\Gamma_d}$ define the tangential directions. At the interface, displacements are allowed to exhibit a discontinuity, and the jump in displacements can be decomposed in the local coordinate system in a normal jump $[\![u_n]\!]$ and in slidings $[\![u_s]\!]$ and $[\![u_t]\!]$:

$$[\![\mathbf{u}]\!] = [\![u_n]\!]\mathbf{n}_{\Gamma_d} + [\![u_s]\!]\mathbf{s}_{\Gamma_d} + [\![u_t]\!]\mathbf{t}_{\Gamma_d}. \tag{2}$$

The rotation matrix $\mathbf{R} = \left[\mathbf{n}^{\mathrm{T}}_{\Gamma_d}, \mathbf{s}^{\mathrm{T}}_{\Gamma_d}, \mathbf{t}^{\mathrm{T}}_{\Gamma_d}\right]$ transforms quantities expressed in the local coordinate system of the interface to the global coordinate system.

At the interface Γ_d, the hydraulic pore pressure p is assumed to be continuous, but its gradient can be discontinuous across Γ_d:

$$\nabla p \cdot \mathbf{n}_{\Gamma_d} \neq 0\,, \tag{3}$$

with $\mathbf{n}_{\Gamma_d}$ the normal to the interface Γ_d; see also Figure 1. These assumptions are rather strong and considerably influence the flow in and around the crack. However, they are appropriate for a large number of applications and for the present case where the crack opening remains small compared with the other dimensions.

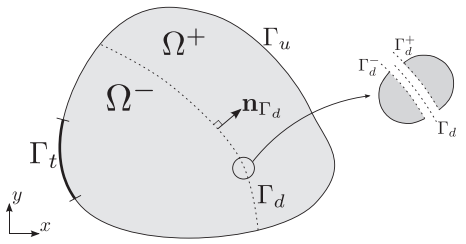

Figure 1. Schematic representation of a body Ω crossed by a discontinuity Γ_d.

DOI: 10.1002/nme

2.2. Balance of momentum and constitutive equations for the solid phase

At time t, the balance of momentum of the mixture takes the following form:

$$\nabla \cdot \boldsymbol{\sigma}(\mathbf{x}, t) = \mathbf{0}, \qquad \mathbf{x} \in \Omega, \tag{4a}$$

$$\mathbf{u}(\mathbf{x}, t) = \bar{\mathbf{u}}(\mathbf{x}, t) \qquad \mathbf{x} \in \Gamma_u, \tag{4b}$$

$$\mathbf{n}_{\Gamma_t}(\mathbf{x}) \cdot \boldsymbol{\sigma}(\mathbf{x}, t) = \bar{\mathbf{t}}(\mathbf{x}, t) \qquad \mathbf{x} \in \Gamma_t, \tag{4c}$$

$$\mathbf{n}_{\Gamma_d}(\mathbf{x}) \cdot \boldsymbol{\sigma}(\mathbf{x}, t) = \mathbf{t}_d\left(\llbracket \mathbf{u} \rrbracket(\mathbf{x}, t)\right) \qquad \mathbf{x} \in \Gamma_d. \tag{4d}$$

The displacements prescribed on the Dirichlet boundary Γ_u are denoted by $\bar{\mathbf{u}}$; the tractions applied to the Neumann boundary Γ_t with normal $\mathbf{n}_{\Gamma_t}$ are denoted by $\bar{\mathbf{t}}$, and $\mathbf{t}_d$ is the interface traction.

In Equation (4), $\boldsymbol{\sigma}$ defines the total stress of the mixture. Under the assumption that the Biot coefficient equals 1, the total stress then follows from

$$\boldsymbol{\sigma} = \boldsymbol{\sigma}^e - p\mathbf{I}, \tag{5}$$

where $\boldsymbol{\sigma}^e$ is the effective stress describing the stress state in the solid skeleton, which is determined by assuming linear elastic behaviour so that

$$\boldsymbol{\sigma}^e = \mathbf{D} : \boldsymbol{\epsilon}, \tag{6}$$

where $\mathbf{D}$ is the elastic stiffness tensor of the solid skeleton.

2.3. Interface behaviour

Substitution of Equation (5) into Equation (4d) shows that the total traction at the interface

$$\mathbf{t}_d = (\boldsymbol{\sigma}^e - p\mathbf{I}) \cdot \mathbf{n}_{\Gamma_d} = \tilde{\mathbf{t}}_d - p\mathbf{n}_{\Gamma_d} \tag{7}$$

is the sum of the traction on the solid skeleton, $\tilde{\mathbf{t}}_d$, and the pore pressure projected onto the interface. The traction at the interface can be a nonlinear function of the displacement jump $\llbracket \mathbf{u} \rrbracket$, i.e. $\mathbf{t}_d = \mathbf{t}_d(\llbracket \mathbf{u} \rrbracket)$, but in the present contribution, we confine ourselves to interfaces that are either intact (zero compliance interfaces) or fully broken. In the local coordinate system of the interface, the traction, which satisfies the relation $\tilde{\mathbf{t}}_d^l = \mathbf{R}\tilde{\mathbf{t}}_d$, takes the form

$$\tilde{\mathbf{t}}_d^l = \mathbf{D}_i \llbracket \mathbf{u} \rrbracket = \begin{bmatrix} k_n & 0 & 0 \\ 0 & k_s & 0 \\ 0 & 0 & k_t \end{bmatrix} \begin{Bmatrix} \llbracket u_n \rrbracket \\ \llbracket u_s \rrbracket \\ \llbracket u_t \rrbracket \end{Bmatrix}. \tag{8}$$

A zero compliance corresponds to infinite 'dummy' stiffnesses k_n, k_s and k_t. In practice, this is achieved by assigning values as high as possible, although it is noted that the magnitude of the dummy stiffnesses is problem and length-scale dependent [35]. The fully broken state, which corresponds to an open crack, is modelled by setting $\mathbf{D}_i = \mathbf{0}$.

2.4. Global mass balance and constitutive equation for the fluid phase

The balance of mass of the mixture takes the following form:

$$\nabla \cdot \mathbf{v}(\mathbf{x}, t) + \frac{1}{M}\frac{\partial p(\mathbf{x}, t)}{\partial t} + \nabla \cdot \mathbf{q}(\mathbf{x}, t) = 0 \qquad \mathbf{x} \in \Omega, \tag{9a}$$

$$\mathbf{q}(\mathbf{x}, t) = \bar{\mathbf{q}}(\mathbf{x}, t) \qquad \mathbf{x} \in \Gamma_q, \tag{9b}$$

$$p(\mathbf{x}, t) = \bar{p}(\mathbf{x}, t) \qquad \mathbf{x} \in \Gamma_p, \tag{9c}$$

$$\mathbf{q}(\mathbf{x}, t) = \mathbf{q}_d(\mathbf{x}, t) \qquad \mathbf{x} \in \Gamma_d. \tag{9d}$$

The vector $\mathbf{v}$ refers to the velocity of the solid skeleton, and $\frac{1}{M}$ is the compressibility modulus. In Equation (9), $\bar{\mathbf{q}}$ denotes the fluid flux that is prescribed on the Neumann boundary Γ_q, while $\bar{p}$ is the prescribed pressure on the Dirichlet boundary Γ_p. We next introduce Darcy's relation for fluid flow in an isotropic porous medium,

DOI: 10.1002/nme

$$\mathbf{q} = -k \nabla p, \tag{10}$$

with k the hydraulic permeability, and rewrite Equation (9a) as

$$\nabla \cdot \mathbf{v}(\mathbf{x}, t) + \frac{1}{M} \frac{\partial p(\mathbf{x}, t)}{\partial t} - \nabla \cdot (k \nabla p(\mathbf{x}, t)) = 0 \qquad \mathbf{x} \in \Omega . \tag{11}$$

In the remainder, the explicit dependence of quantities on the spatial and time coordinates $(\mathbf{x}, t)$ will be omitted for notational simplicity.

3. MESHES OF DIFFERENT ORDER

In this contribution, the spatial discretisation is carried out using NURBS, the shape functions commonly used in isogeometric analysis, in lieu of Lagrange polynomials that are used in standard finite element analysis. A major advantage of isogeometric analysis is that the use of shape functions of order p allow to obtain an interelement continuity of an order up to $\mathcal{C}^{p-1}$. This is a direct consequence of the fact that NURBS, and also the underlying B-splines, normally extend over more than one element. In order to cast this formulation into a standard finite element data structure, we employ the Bézier extraction operator [34, 38]. This operator is constant for each element and expresses the NURBS as a linear combination of Bernstein polynomials of order p, which only span one element.

Biphasic models do not necessarily satisfy the Ladyzhenskaya–Babuška–Brezzi-condition [31, 32], and may exhibit oscillatory behaviour in the spatial distribution of pore pressures for consolidation-type problems. This condition is often satisfied when the approximation order of the displacement field is chosen one degree higher than the approximation order of the pressure field [33]. In standard finite element analysis, it is relatively straightforward to generate meshes that have interpolations of different orders within an element, for example, using the Taylor–Hood elements. The corner nodes are then equipped with degrees of freedom for the displacements as well as for the pressures, while the other nodes typically only support displacement degrees of freedom. With isogeometric analysis, it is more complicated to generate meshes that have different orders of interpolation with matching element boundaries, which is an essential feature to carry out the numerical integration of the force vectors and stiffness matrices.

As a point of departure, we take the p-refinement algorithm presented in [36] to generate meshes with interpolants of different order. The examples presented in the following section are restricted to a two-dimensional setting and to quadratic interpolants for the approximation of the pressure field and to cubic interpolants for the approximation of the displacements. This is sufficient for the discretisation of the pressure field in the crack, which involves second derivatives of the pressure [15, 17, 18], and to satisfy the *inf–sup* condition.

First, the univariate degree elevation matrix $\mathbf{E}_{\text{uni}}^{p,p'}$ is constructed, which enables to p-refine a quadratic mesh ($p = 2$) to a cubic mesh ($p' = 3$)

$$\mathbf{E}_{\text{uni}}^{2,3} = \begin{bmatrix} 1 & \frac{1}{3} & 0 & 0 \\ 0 & \frac{2}{3} & \frac{2}{3} & 0 \\ 0 & 0 & \frac{1}{3} & 1 \end{bmatrix}. \tag{12}$$

This operator is constant for elevation from p to p' and therefore has to be evaluated only once. The bivariate degree elevation matrix is obtained as the product of the univariate elevation matrices, defined in [38]:

$$\mathbf{E}^{2,3} = \mathbf{E}_{\text{uni}}^{2,3} \otimes \mathbf{E}_{\text{uni}}^{2,3}. \tag{13}$$

Finally, the Bézier projection, which has to be carried out for each element e, is employed to express the coordinates of the control points of the cubic mesh $\mathbf{P}^{e,3}$ as a function of those of the quadratic mesh $\mathbf{P}^{e,2}$:

$$\mathbf{P}^{e,3} = \left(\mathbf{R}^{e,3}\right)^{\mathrm{T}} \left(\mathbf{E}^{2,3}\right)^{\mathrm{T}} \left(\mathbf{C}^{e,2}\right)^{\mathrm{T}} \mathbf{P}^{e,2}. \tag{14}$$

DOI: 10.1002/nme

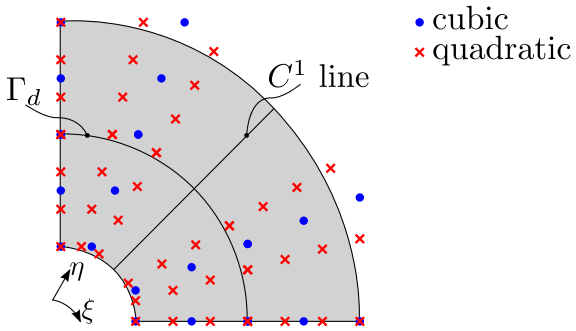

Figure 2. Example of a 2×2-element non-uniform rational basis spline mesh with quadratic and cubic control points.

In Equation (14), $\mathbf{C}^{e,2}$ is the Bézier extraction operator of the quadratic element e, cf. [28], while the reconstruction operator $\mathbf{R}^{e,3}$ is the inverse of $\mathbf{C}^{e,3}$, the Bézier extraction operator of the cubic element e.

As an example, we consider the NURBS geometry depicted in Figure 2, which consists of two elements in the η as well as in the ξ-direction. The quadratic knot vectors read

$$\xi^2 = \left[0, 0, 0, \frac{1}{2}, 1, 1, 1\right]$$
$$\eta^2 = \left[0, 0, 0, \frac{1}{2}, \frac{1}{2}, \frac{1}{2}, 1, 1, 1\right],$$

where the repeated value $\frac{1}{2}$ in η^2 characterises the discontinuity Γ_d. The knot vectors of the matching cubic mesh are

$$\xi^3 = \left[0, 0, 0, 0, \frac{1}{2}, \frac{1}{2}, 1, 1, 1, 1\right]$$
$$\eta^3 = \left[0, 0, 0, 0, \frac{1}{2}, \frac{1}{2}, \frac{1}{2}, \frac{1}{2}, 1, 1, 1, 1\right].$$

It is emphasised that upon degree elevation, the multiplicity of each knot has to be increased accordingly in order to ensure identical interelement continuity for both meshes. This is necessary to achieve matching element boundaries. The control point coordinates of the mesh shown in Figure 2 are given in the Appendix.

4. WEAK FORMULATION AND MASS COUPLING

4.1. Momentum balance

In order to cast the momentum balance, Equation (4a), in a weak format, it is in a standard fashion multiplied by a virtual displacement field $\delta\mathbf{u}$, followed by application of the divergence theorem and use of the boundary conditions, Equations (4b)– (4d):

$$\int_\Omega \nabla\delta\mathbf{u} : \boldsymbol{\sigma}\, \mathrm{d}V - \int_{\Gamma_d^+} \delta\mathbf{u}^+ \cdot \mathbf{t}_d^+\, \mathrm{d}A - \int_{\Gamma_d^-} \delta\mathbf{u}^- \cdot \mathbf{t}_d^-\, \mathrm{d}A = \int_{\Gamma_t} \delta\mathbf{u} \cdot \bar{\mathbf{t}}\, \mathrm{d}A\,. \tag{15}$$

In Equation (15), the integrals at the discontinuity can be gathered owing to the property $\Gamma_d = \Gamma_d^+ = \Gamma_d^-$, which defines a zero-thickness interface. In addition, using $\mathbf{n}_{\Gamma_d} = \mathbf{n}_{\Gamma_d}^- = -\mathbf{n}_{\Gamma_d}^+$, see also Figure 1, and requiring that the total traction is continuous across the interface, i.e. $\mathbf{t}_d = \mathbf{t}_d^- = -\mathbf{t}_d^+$, leads to

$$\int_\Omega \delta\boldsymbol{\epsilon} : (\boldsymbol{\sigma}^e - p\mathbf{I})\, \mathrm{d}V + \int_{\Gamma_d} [\![\delta\mathbf{u}]\!] \cdot \underbrace{(\tilde{\mathbf{t}}_d - p\mathbf{I}\mathbf{n}_{\Gamma_d})}_{\mathbf{t}_d = \boldsymbol{\sigma}\cdot\mathbf{n}_{\Gamma_d}}\, \mathrm{d}A = \int_{\Gamma_t} \delta\mathbf{u} \cdot \bar{\mathbf{t}}\, \mathrm{d}A\,, \tag{16}$$

DOI: 10.1002/nme

with $[\![\delta\mathbf{u}]\!]$ as the virtual displacement jump. The virtual strain tensor $\delta\boldsymbol{\varepsilon}$ is derived using the assumption of small displacement gradients. Note that it is a direct consequence of the assumption of a constant total traction across the interface that the hydraulic pressure is constant across Γ_d, i.e. $p^+ = p^-$, cf. [39, 40]. This assumption implies that there is no Darcy-driven flow across the interface and, in particular, across a potentially open cavity ($[\![\mathbf{u}]\!] > 0$). However, as has been shown in [15, 17] and recapitulated in a subsequent section, this does not prevent fluid to flow into a crack, where it can be stored, e.g. through crack opening, or be transported within the crack. Therefore, the normal fluid flow can experience a discontinuity.

For each element e the displacement field $\mathbf{u}$, the pressure field p and the displacement jump $[\![\mathbf{u}]\!]$ are now interpolated as follows:

$$\mathbf{u} = \mathbf{N}_u \mathbf{u}^e, \tag{17a}$$

$$p = \mathbf{N}_p \mathbf{p}^e, \tag{17b}$$

$$[\![\mathbf{u}]\!] = \mathbf{M}_u \mathbf{u}^e. \tag{17c}$$

All operators in Equation (17) contain isogeometric shape functions: the matrices $\mathbf{N}_u$ and $\mathbf{M}_u$ contain the shape function related to the displacement degrees of freedom (cf. [34, 35] for details to build the jump operator $\mathbf{M}_u$), while $\mathbf{N}_p$ contains the shape functions related to the interpolation of the pressure field. From Equation (17a), the strains in the body Ω can be derived by standard differentiation of the isogeometric shape functions so that

$$\boldsymbol{\epsilon} = \mathbf{B}_u \mathbf{u}^e, \tag{18}$$

with $\mathbf{B}_u$ as the standard strain-nodal displacement operator. Upon substitution of the interpolations of Equation (17) and requiring that the resulting set of algebraic equations holds for all kinematically admissible $\delta\mathbf{u}$, the discrete equilibrium equation is obtained:

$$\mathbf{f}_U^{\text{int}} = \mathbf{f}_U^{\text{ext}}, \tag{19}$$

with the external force vector

$$\mathbf{f}_U^{\text{ext}} = \int_{\Gamma_t} \mathbf{N}_u^{\mathrm{T}} \bar{\mathbf{t}} \, \mathrm{d}A \tag{20}$$

and the corresponding internal force vector

$$\begin{aligned} \mathbf{f}_U^{\text{int}} = \int_\Omega \mathbf{B}_u^{\mathrm{T}} \mathbf{D}_b \mathbf{B}_u \mathbf{u}^e \, \mathrm{d}V - \int_\Omega \mathbf{B}_u^{\mathrm{T}} \mathbf{m} \mathbf{N}_p \mathbf{p}^e \, \mathrm{d}V \quad \dots \\ + \int_{\Gamma_d} \mathbf{M}_u^{\mathrm{T}} \mathbf{D}_i \mathbf{M}_u \mathbf{u}^e \, \mathrm{d}A - \int_{\Gamma_d} \mathbf{M}_u^{\mathrm{T}} \mathbf{n}_{\Gamma_d} \mathbf{N}_p \mathbf{p}^e \, \mathrm{d}A. \end{aligned} \tag{21}$$

In the second term on the right-hand side of Equation (21), the operator $\mathbf{m} = [1\ 1\ 0]^{\mathrm{T}}$ was introduced to build the hydrostatic pressure term $p\mathbf{I}$ in Voigt's notation.

Linearisation of the internal force vector $\mathbf{f}_U^{\text{int}}$ results in

$$\mathbf{K}_{uu} = \frac{\partial \mathbf{f}_U^{\text{int}}}{\partial \mathbf{u}^e} = \underbrace{\int_\Omega \mathbf{B}_u^{\mathrm{T}} \mathbf{D}_b \mathbf{B}_u \, \mathrm{d}V}_{\mathbf{K}_{uu}^{\Omega}} + \underbrace{\int_{\Gamma_d} \mathbf{M}_u^{\mathrm{T}} \mathbf{D}_i \mathbf{M}_u \, \mathrm{d}A}_{\mathbf{K}_{uu}^{\Gamma_d}} \tag{22a}$$

$$\mathbf{K}_{up} = \frac{\partial \mathbf{f}_U^{\text{int}}}{\partial \mathbf{p}^e} = -\underbrace{\int_\Omega \mathbf{B}_u^{\mathrm{T}} \mathbf{m} \mathbf{N}_p \, \mathrm{d}V}_{\mathbf{K}_{up}^{\Omega}} - \underbrace{\int_{\Gamma_d} \mathbf{M}_u^{\mathrm{T}} \mathbf{n}_{\Gamma_d} \mathbf{N}_p \, \mathrm{d}A}_{\mathbf{K}_{up}^{\Gamma_d}}. \tag{22b}$$

4.2. Mass balance

The weak form of the mass balance is derived in a similar manner as that of the momentum balance, namely, by multiplying the mass balance, Equation (9a), by a virtual pressure δp and integrating

DOI: 10.1002/nme

over the body Ω. Subsequently, the divergence theorem is applied and the boundary conditions, Equations (9b)–(9d) are exploited. With the assumption that the pressure is continuous across the interface and adopting a Bubnov–Galerkin approach, so that also $\delta p^+ = \delta p^- = \delta p$, we obtain

$$\begin{aligned}&\int_\Omega \delta p \nabla\cdot\mathbf{v} + \frac{1}{M}\delta p\frac{\partial p}{\partial t} + \nabla\delta p\cdot(k\nabla p)\,\mathrm{d}V + \dots \\ &+ \int_{\Gamma_d^+} \delta p\,\mathbf{q}_d^+\cdot\mathbf{n}_{\Gamma_d^+}\,\mathrm{d}A + \int_{\Gamma_d^-}\delta p\,\mathbf{q}_d^-\cdot\mathbf{n}_{\Gamma_d^-}\,\mathrm{d}A = -\int_{\Gamma_q}\delta p\,\mathbf{q}_p\cdot\mathbf{n}_{\Gamma_q}\,\mathrm{d}A\,.\end{aligned} \tag{23}$$

Like for the balance of momentum, the integrals along the interface are gathered using $\Gamma_d = \Gamma_d^+ = \Gamma_d^-$ and $\mathbf{n}_{\Gamma_d} = \mathbf{n}_{\Gamma_d}^- = -\mathbf{n}_{\Gamma_d}^+$, so that

$$\int_\Omega \delta p\nabla\cdot\mathbf{v} + \frac{1}{M}\delta p\frac{\partial p}{\partial t} + \nabla\delta p\cdot(k\nabla p)\,\mathrm{d}V - \int_{\Gamma_d}\delta p\,[\![\mathbf{q}_d]\!]\cdot\mathbf{n}_{\Gamma_d}\,\mathrm{d}A = -\int_{\Gamma_q}\delta p\,\mathbf{q}_p\cdot\mathbf{n}_{\Gamma_q}\,\mathrm{d}A. \tag{24}$$

A jump in the flux $[\![\mathbf{q}_d]\!]$ has now emerged in the integral for the interface. Furthermore, this term is multiplied by the normal $\mathbf{n}_{\Gamma_d}$ to Γ_d, resulting in a jump of the flow normal to the interface. This means that the flow can be discontinuous at Γ_d as some of the fluid that flows into the crack can be stored or be transported within the crack. The jump in the flux is therefore a measure of the net fluid exchange between an open discontinuity (a cavity) and the surrounding bulk material.

From the discretisations introduced in Equation (17), the gradients of pressure p are computed as

$$\nabla p = \mathbf{B}_p\mathbf{p}^e, \tag{25}$$

where $\mathbf{B}_p$ contains the derivatives of the shape functions for the pressure. Substitution of Equations (17b) and (25) allows rewriting Equation (24) in a discrete format:

$$\begin{aligned}&\int_\Omega \mathbf{N}_p^{\mathrm{T}}\mathbf{m}^{\mathrm{T}}\mathbf{B}_u\dot{\mathbf{u}}^e\,\mathrm{d}V + \int_\Omega\frac{1}{M}\mathbf{N}_p^{\mathrm{T}}\mathbf{N}_p\dot{\mathbf{p}}^e\,\mathrm{d}V + \int_\Omega k\mathbf{B}_p^{\mathrm{T}}\mathbf{B}_p\mathbf{p}^e\,\mathrm{d}V + \dots \\ &\qquad \underbrace{-\int_{\Gamma_d}\mathbf{N}_p^{\mathrm{T}}\,\mathbf{n}_{\Gamma_d}^{\mathrm{T}}[\![\mathbf{q}_d]\!]\,\mathrm{d}A}_{\mathbf{Q}^{\Gamma_d}} = -\int_{\Gamma_q}\mathbf{N}_p^{\mathrm{T}}\,\mathbf{n}_{\Gamma_q}^{\mathrm{T}}\bar{\mathbf{q}}\,\mathrm{d}A\,,\end{aligned} \tag{26}$$

where $\mathbf{Q}^{\Gamma_d}$ is the rate of fluid exchange between the cavity and the bulk.

The integration over a time step Δt is carried out using a finite difference scheme:

$$\dot{(\bullet)} = \frac{(\bullet)^{t+\Delta t} - (\bullet)^t}{\Delta t}. \tag{27}$$

Substitution of the time integration scheme, Equation (27), into Equation (26) and multiplying the result by $-\Delta t$ in order to retain a symmetrical stiffness matrix leads to

$$\mathbf{f}_P^{\mathrm{int}} = \mathbf{f}_P^{\mathrm{ext}} \tag{28}$$

with the external force vector

$$\mathbf{f}_P^{\mathrm{ext}} = \Delta t\int_{\Gamma_q}\mathbf{N}_p^{\mathrm{T}}\,\mathbf{n}_{\Gamma_q}^{\mathrm{T}}\bar{\mathbf{q}}\,\mathrm{d}A \tag{29}$$

and the internal force vector

$$\mathbf{f}_P^{\mathrm{int}} = \left(\mathbf{K}_{up}^\Omega\right)^{\mathrm{T}}\mathbf{u}^{t+\Delta t} + \mathbf{K}_{pp}^\Omega\mathbf{p}^{t+\Delta t} - \left(\mathbf{K}_{up}^\Omega\right)^{\mathrm{T}}\mathbf{u}^t - \int_\Omega\frac{1}{M}\mathbf{N}_p^{\mathrm{T}}\mathbf{N}_p\,\mathrm{d}V\mathbf{p}^t + \Delta t\mathbf{Q}^{\Gamma_d} \tag{30}$$

DOI: 10.1002/nme

The submatrix $\mathbf{K}_{pp}^{\Omega}$ is defined as

$$\mathbf{K}_{pp}^{\Omega} = -\int_{\Omega} \frac{1}{M} \mathbf{N}_p^{\mathrm{T}} \mathbf{N}_p \, \mathrm{d}V - \Delta t \int_{\Omega} k \mathbf{B}_p^{\mathrm{T}} \mathbf{B}_p \, \mathrm{d}V. \tag{31}$$

The complete linearised set of equations, needed in a Newton–Raphson framework, then reads

$$\begin{bmatrix} \mathbf{K}_{uu}^{\Omega} + \mathbf{K}_{uu}^{\Gamma_d} & \mathbf{K}_{up}^{\Omega} + \mathbf{K}_{up}^{\Gamma_d} \\ \left(\mathbf{K}_{up}^{\Omega}\right)^{\mathrm{T}} & \mathbf{K}_{pp}^{\Omega} \end{bmatrix} \begin{Bmatrix} d\mathbf{u} \\ d\mathbf{p} \end{Bmatrix} = \begin{Bmatrix} \mathbf{f}_U^{\mathrm{ext}} \\ \mathbf{f}_P^{\mathrm{ext}} \end{Bmatrix} - \begin{Bmatrix} \mathbf{f}_U^{\mathrm{int}} \\ \mathbf{f}_P^{\mathrm{int}} \end{Bmatrix}, \tag{32}$$

with the symbol d denoting the iterative change from one iteration to the next. It is noted that the term $\mathbf{K}_{up}^{\Gamma_d}$ renders the global stiffness matrix unsymmetrical and will be omitted in the simulations.

4.3. Mass coupling

In this section, we briefly recapitulate the derivation of $\mathbf{Q}_{\Gamma_d}$, which characterises the jump in fluid flow at the interface Γ_d in Equation (26); see [15] for all details. The geometry of the cavity, i.e. the open crack, is shown in Figure 3. It is assumed that at any point $\mathbf{x}$ along the interface Γ_d, the opening of the cavity,

$$2h = [\![\mathbf{u}]\!](\mathbf{x}) \tag{33}$$

remains small in comparison with its length. Moreover, phenomena at the tip of the cavity are neglected. This allows to consider a quasi one-dimensional flow in the tangential direction $\mathbf{s}_{\Gamma_d}$ of the aperture, which is in line with the assumption made in previous sections where the pressure was considered constant across the cavity, i.e. $p^+(\mathbf{x}) = p^-(\mathbf{x})$.

The projection of the flux jump in the normal direction can be expressed as

$$\mathbf{n}_{\Gamma_d}^{\mathrm{T}} [\![\mathbf{q}_d]\!] = n_f [\![w_f - w_s]\!], \tag{34}$$

where the terms $w_\alpha = \mathbf{v}_\alpha \cdot \mathbf{n}_{\Gamma_d}$ are the solid normal velocity ($\alpha = S$) and the fluid normal velocity ($\alpha = F$). The jump in the solid velocity in the normal direction is simply evaluated as

$$[\![w_s]\!] = 2\frac{\partial h}{\partial t}. \tag{35}$$

Without loss of generality, the jump in fluid velocity can be expressedas

$$[\![w_f]\!] = -\int_{-h}^{h} \frac{\partial w_f}{\partial y_d} \, \mathrm{d}y_d. \tag{36}$$

This term can be evaluated by considering fluid flow at the length scale of the cavity. This will be referred to as the 'micro-flow', as it describes a process taking place at a length scale that is orders

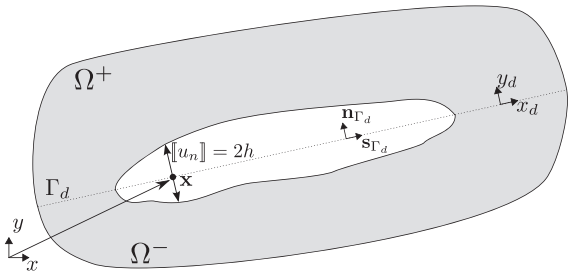

Figure 3. Geometry of an open interface Γ_d.

DOI: 10.1002/nme

of magnitude smaller than the flow in the bulk. Assuming a Newtonian fluid (although the extension to, e.g. power-law fluids is rather straightforward), the momentum balance for this micro-flow can be projected in the tangential direction and integrated in the normal direction to obtain the tangential fluid velocity profile in the cavity:

$$v_f(y_d) = \frac{1}{2\mu}\frac{\partial p}{\partial x_d}(y_d^2 - h^2) + v_f^{\pm} \,. \tag{37}$$

The term $v_f^{\pm}$ corresponds to the fluid velocity at the faces of the discontinuity. The balance of mass can also be evaluated for the fluid in the cavity. Assuming small changes in fluid density, this gives

$$\frac{\partial v_f}{\partial x_d} + \frac{\partial w_f}{\partial y_d} = 0 \,. \tag{38}$$

Using the projection of Darcy's law in the direction tangential to the discontinuity

$$v_f = \left(\mathbf{v}_s - \frac{k}{n_f}\nabla p\right)\cdot \mathbf{s}_{\Gamma_d} \tag{39}$$

and substituting Equations (37) and (38) back into Equation (36) allows to evaluate the jump in fluid velocity $[\![w_f]\!]$. Together with Equation (35), this leads to an expression for the normal jump in fluid flow at the interface:

$$\mathbf{n}_{\Gamma_d}^{\mathrm{T}}[\![\mathbf{q}_d]\!] = \frac{n_f}{12\mu}\frac{\partial^2 p}{\partial x_d^2}(2h)^3 + \frac{n_f}{4\mu}\frac{\partial p}{\partial x_d}\frac{\partial (2h)}{\partial x_d}(2h)^2 - 2h\left(n_f\frac{\partial v_s}{\partial x_d} - k_f\frac{\partial^2 p}{\partial x_d^2}\right) - n_f\frac{\partial (2h)}{\partial t}. \tag{40}$$

It is important to notice that $\mathbf{Q}^{\Gamma_d}$ is a measure of the gain or loss of fluid in the cavity. As Equation (40) shows, fluid exchange between a cavity and its surrounding bulk can only take place when a cavity has started to form, i.e. when $2h > 0$. Furthermore, Equation (40) shows that the jump in the normal flow is driven by gradients in the tangential direction x_d. Finally, it is noticed that the second derivative of the pressure field is required in the implementation of the model. This implies that the interpolation functions for the pressure must be at least quadratic.

Further to Equations (17) and (25), additional discretisations are needed for the second gradient of the pressure, as well as for the jump gradients at the interface:

$$\nabla(\nabla p) = \mathbf{B}_p^2\mathbf{p}^e \tag{41a}$$

$$\nabla[\![\mathbf{u}]\!] = \mathbf{G}_u\mathbf{u}^e. \tag{41b}$$

Equation (40) also requires the evaluation of the tangential gradient of the solid velocity in the cavity and is approximated as the average of the velocities between Γ_d^+ and Γ_d^-:

$$\frac{\partial v_s}{\partial x_d} \approx \mathbf{s}_{\Gamma_d}^{\mathrm{T}}\cdot\langle\mathbf{B}_u\rangle\dot{\mathbf{u}}^e\cdot\mathbf{s}_{\Gamma_d}, \tag{42}$$

where the operator $\langle\mathbf{B}_u\rangle$ is built similar to $\mathbf{M}_u$, but replacing the shape functions with their gradients, and the coefficients ± 1 with $\frac{1}{2}$. Finally, the rate of fluid flow in the cavity is given by

$$\mathbf{Q}^{\Gamma_d} = \int_{\Gamma_d}\mathbf{N}_p^{\mathrm{T}}\,\mathbf{n}_{\Gamma_d}^{\mathrm{T}}[\![\mathbf{q}_d]\!]\,\mathrm{d}A, \tag{43}$$

where

$$\begin{aligned}\mathbf{n}_{\Gamma_d}^{\mathrm{T}}[\![\mathbf{q}_d]\!] =& \frac{n_f}{12\mu}\left(\mathbf{s}_{\Gamma_d}^{\mathrm{T}}\cdot\mathbf{B}_p^2\mathbf{p}^e\cdot\mathbf{s}_{\Gamma_d}\right)\left(\mathbf{n}_{\Gamma_d}^{\mathrm{T}}\cdot\mathbf{M}_u\mathbf{u}^e\right)^3\ldots\\ &+\frac{n_f}{4\mu}\left(\mathbf{s}_{\Gamma_d}^{\mathrm{T}}\cdot\mathbf{B}_p\mathbf{p}^e\right)\left(\mathbf{n}_{\Gamma_d}^{\mathrm{T}}\cdot\mathbf{G}_u\mathbf{u}^e\cdot\mathbf{s}_{\Gamma_d}\right)\left(\mathbf{n}_{\Gamma_d}^{\mathrm{T}}\cdot\mathbf{M}_u\mathbf{u}^e\right)^2\ldots\\ &-\left(\mathbf{n}_{\Gamma_d}^{\mathrm{T}}\cdot\mathbf{M}_u\mathbf{u}^e\right)\left(n_f\cdot\langle\mathbf{B}_u\rangle\dot{\mathbf{u}}^e\cdot\mathbf{s}_{\Gamma_d} - k_f\cdot\mathbf{B}_p^2\mathbf{p}^e\cdot\mathbf{s}_{\Gamma_d}\right)^{\mathrm{T}}\cdot\mathbf{s}_{\Gamma_d}\ldots\\ &-n_f\mathbf{n}_{\Gamma_d}^{\mathrm{T}}\cdot\mathbf{M}_u\dot{\mathbf{u}}^e.\end{aligned} \tag{44}$$

DOI: 10.1002/nme

The contributions $\frac{\partial \mathbf{Q}^{\Gamma_d}}{\partial \mathbf{u}^e}$ and $\frac{\partial \mathbf{Q}^{\Gamma_d}}{\partial \mathbf{p}^e}$ to the global tangential stiffness matrix are again omitted to preserve symmetry.

5. INTEGRATION OF THE POROMECHANICAL INTERFACE ELEMENT

The numerical integration along the interface Γ_d requires special attention, and we recall the contributions to the internal internal force vector; see Equations (21) and (30):

$$\mathbf{f}_U^{\text{int}}\Big|_{\Gamma_d} = \int_{\Gamma_d} \mathbf{M}_u^{\mathrm{T}} \mathbf{D}_i \mathbf{M}_u \mathbf{u}^e - \mathbf{M}_u^{\mathrm{T}} \mathbf{n}_{\Gamma_d} \mathbf{N}_p \mathbf{p}^e \; \mathrm{d}A \;, \tag{45a}$$

$$\mathbf{f}_P^{\text{int}}\Big|_{\Gamma_d} = \int_{\Gamma_d} \mathbf{N}_p^{\mathrm{T}} \, \mathbf{n}_{\Gamma_d}^{\mathrm{T}} [\![\mathbf{q}_d]\!] \, \mathrm{d}A. \tag{45b}$$

Zero-thickness interface elements tend to introduce oscillations in the traction profile along the interface when Gauss quadrature is used to approximate integrals on Γ_d [41, 42]. This is the case for a single-phase formulation, where only the first term of Equation (45a) is present. In the following, this term will be referred to as the 'solid interface term'. These oscillations are commonly removed in standard finite element analysis by resorting to a Newton–Cotes integration scheme, but cannot be suppressed in this way for interface elements that use B-splines or NURBS [34]. In [35], it has been argued that the use of lumped integration at the interface (i.e. at set of control points) may be the only way to avoid this spurious behaviour.

The formulation of the biphasic problem gives rise to two additional terms at the interface, namely, the second term in Equation (45a) and (45b), which will be referred to as the 'fluid interface terms'. We will now assess whether the fluid interface terms introduced by the biphasic formulation also contribute towards an oscillatory behaviour. Two schemes are considered:

- 'Gauss' refers to Gauss quadrature used for all terms in Equation (45). Data resulting from this scheme are therefore evaluated at the integration points.
- 'Lumped' will refer to a mixed-scheme where lumped integration is used for the solid interface term only, while Gauss integration is employed for the fluid interface terms. Results will either be plotted at the control points or at the Gauss points (post-processing).

We will assess the schemes at the hand of the example of the quarter of a torus shown in Figure 4a. The quadratic mesh presented in Figure 2 was degree elevated to a cubic mesh using the algorithm developed earlier in this paper and refined using the algorithm in [43] as to obtain the mixed 32×32-element mesh of Figure 4. It consists of 2592 control points, 1368 of which relate to the interpolation of the displacements using cubic NURBS and the remaining 1224 control points relate to the interpolation of the pressure using quadratic NURBS.

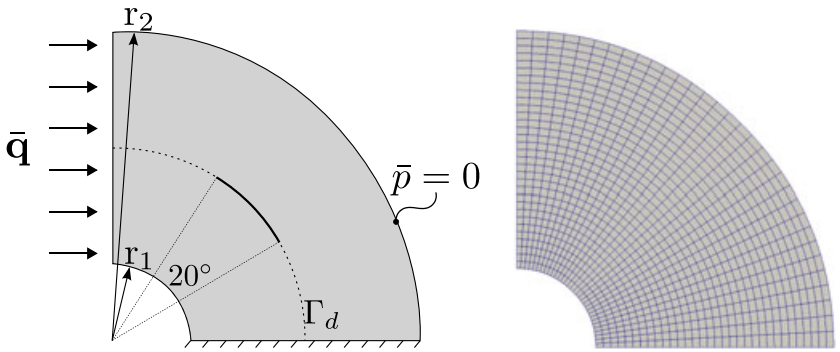

(a) Geometry (b) Mesh

Figure 4. Geometry and mesh of the curved beam, $r_1 = 2.5$ m and $r_2 = 10$ m.

DOI: 10.1002/nme

A biphasic media with a quasi-incompressible fluid $M = 10^{18}$ MPa is considered. The Young's modulus is taken as $E = 9 \cdot 10^3$ MPa and the Poisson ratio equal to $\nu = 0.4$. The dummy stiffnesses at the interface are chosen as $k_n = k_s = 10^5$ MPa. The hydraulic permeability of the solid skeleton

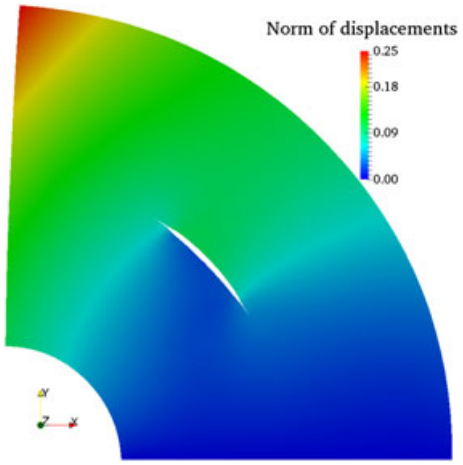

Figure 5. Contour plot of the displacements for the curved beam at time $t = 10$ s magnified by a factor 1500.

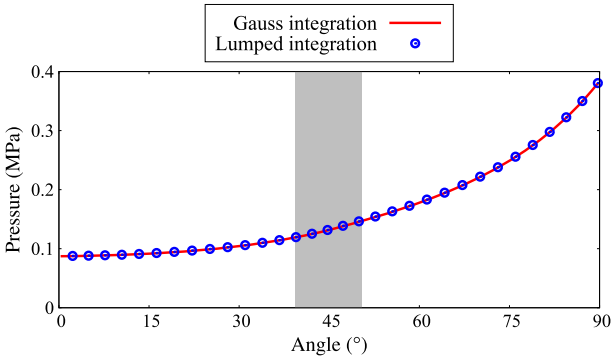

Figure 6. Pressure profile along the interface at time $t = 10$ s. For both integration schemes, the pressure is evaluated at the Gauss points. The grey area shows the location of the crack.

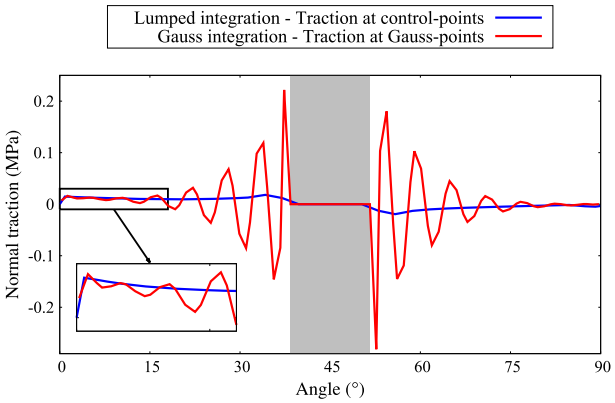

Figure 7. Normal traction along the interface at time $t = 10$ s.

DOI: 10.1002/nme

is taken as $k = 10^3\,\mathrm{mm}^4\,\mathrm{N}^{-1}\mathrm{s}^{-1}$ and the fluid viscosity as $\mu = 10^{-9}\,\mathrm{Nmm}^{-2}\,\mathrm{s}^{-1}$. Finally, the porosity is $n_f = 0.3$.

The interface Γ_d runs in the hoop direction at a radius $0.5(r_1{+}r_2)$. A zero-traction section is located at the centre of the discontinuity over an angle of 20°. The sample is fully fixed at the bottom edge, and the outer radius is an impermeable boundary ($p = 0$). A constant flux $\bar{q} = 0.1\,\mathrm{mm\,s}^{-1}$ is imposed on the left edge.

First, the example shows that the use of meshes of different order works well for this biphasic model. The deformed shape at $t = 10\,\mathrm{s}$ is given in Figure 5, and it can be seen that the cavity has opened under the action of the imposed fluid flow.

Next, it is observed that oscillations only occur in the traction profile along the interface, but not in the pressure profile. Figure 6 shows that, irrespective of the integration scheme that is used, i.e Gauss integration or lumped integration, the pressure distribution is smooth along the interface and is not affected by the integration scheme.

Figure 7 reveals that traction oscillations are also present for the biphasic model when Gauss integration is employed for the numerical integration of all terms in Equation (45). However, with the lumped integration scheme, traction oscillations are not present, whether the traction is evaluated at the control point, or *a posteriori* at the Gauss points (result is not shown here). The calculation thus demonstrates that the solid interface term is the only pathological term regarding oscillatory behaviour, which implies that numerical treatment of the fluid interface terms is not necessary. This is a very positive result as lumped integration of terms such as $\int_{\Gamma_d} \mathbf{M}_u^{\mathrm{T}} \mathbf{n}_{\Gamma_d} \mathbf{N}_p \mathbf{p}^e \,\mathrm{d}A$ would not have been possible with isogeometric analysis because of the non-interpolatory nature of isogeometric meshes.

6. PARAMETER STUDY: SQUARE-PLATE WITH AN INCLINED INTERFACE

In this example, the plate plotted in Figure 8a is considered. It is crossed by a discontinuity inclined at an angle α. Similar to the previous example, the centre part of Γ_d is a zero-traction interface. Also the same material properties have been used as in the previous section.

The fluid velocity in Figure 9 can be evaluated at the centre of the cavity, using the expression derived in Equation (37) for $y_d = 0$. The term $v_f^{\pm}$ is approximated using the projection of Darcy's law in the tangential direction, Equation (39). The solid velocity at the centre of the cavity was taken as the average of the solid velocities on both sides of the discontinuity. Figure 9 shows that for a horizontal crack ($\alpha = 0$), the fluid velocity is symmetric in the cavity, flowing with equal magnitudes to the left and to the right. As the interface inclines, it aligns with the direction of the prescribed flow. As a result, the fluid accelerates more and more in the cavity, which starts to behave like a resistance-free channel for the fluid.

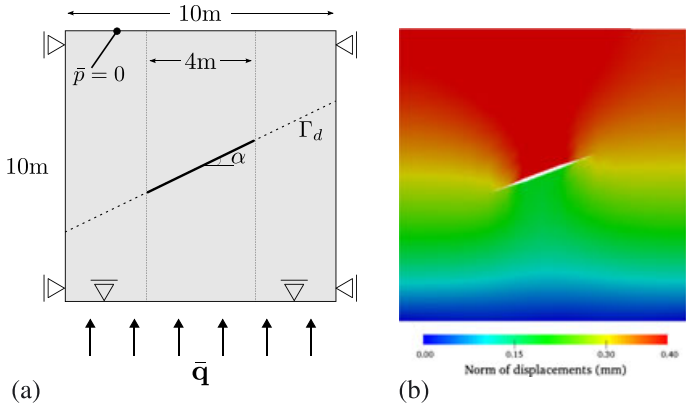

Figure 8. Square plate crossed by an interface with an inclined crack: geometry (a) and contour plot of displacements at steady state, magnified by a factor 500 (b).

DOI: 10.1002/nme

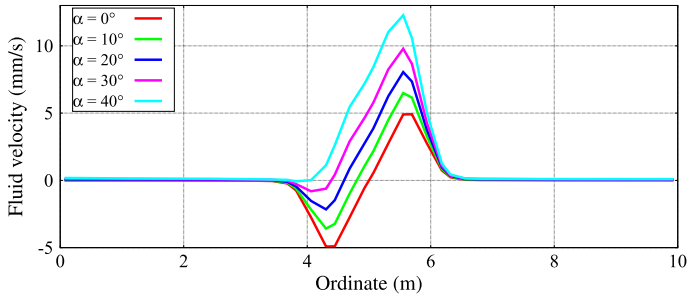

Figure 9. Tangential fluid velocity along the interface at steady state.

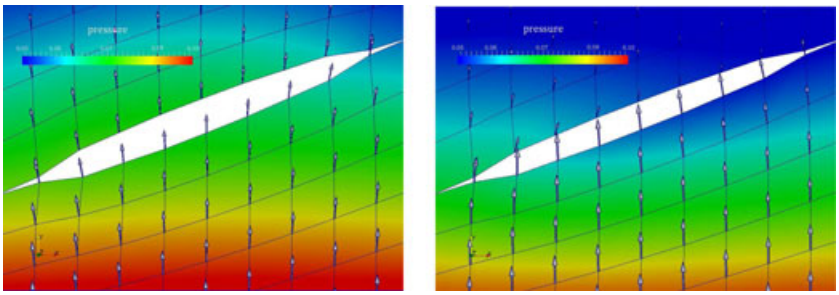

(a) Without 'micro-flow'

(b) With 'micro-flow'

Figure 10. Pressure contour and flux vectors in the vicinity of the opened cavity at $t = 1$ s. It is noted that the figure only shows the flow within the bulk and not within the cavity.

Finally, Figure 10 shows the effects of the 'micro-flow' in the area surrounding the cavity at an early stage of the simulation. When the term $\mathbf{Q}_{\Gamma_d}$ is not active, the flux is the same on both faces of the discontinuity: this absence of a flux jump implies that the fluid flows through the cavity without being affected by its presence. The jump in the fluid flow is clearly visibly in Figure 10. when $\mathbf{Q}^{\Gamma_d}$ is turned on, because the fluid is flowing tangentially along the cavity (although not visible in the figure).

7. CONCLUDING REMARKS

An isogeometric finite element model has been developed for a fluid-saturated porous material, that contains pre-existing cracks. The isogeometric interface elements that describe the cracks can transport fluid, and the fluid flow within the cracks is coupled to the fluid flow in the surrounding porous material via a micro–macro coupling that conserves mass.

To avoid spurious pore pressure distributions in the bulk, an algorithm for unequal order interpolation has been developed in which the displacements are interpolated one order higher than the pressures. Although no formal proof exists that the present scheme indeed satisfies the *inf-sup* condition, numerical experiments indicate a good performance.

Finally, an investigation has been made into spurious traction oscillations that occur for standard and isogeometric interface elements. To avoid such traction oscillations, Gauss integration must be replaced by a lumped integration scheme in the 'solid' parts of the discretised equations. However, it was demonstrated that this is not necessary for the 'fluid' parts, where a standard Gauss scheme can be applied, which greatly facilitates the implementation in isogeometric finite element analysis.

ACKNOWLEDGEMENT

Financial support through the ERC Advanced Grant 664734 'PoroFrac' is gratefully acknowledged.

DOI: 10.1002/nme

APPENDIX

The control points of the mesh presented in Figure 2, with an internal radius of 2500 and external radius of 10 000, are

$$\mathbf{P}^{e,2} = \begin{Bmatrix} 0 & 2500 \\ 1035.5 & 2500 \\ 2500 & 1035.5 \\ 2500 & 0 \\ 0 & 4375 \\ 1812.2 & 4375 \\ 4375 & 1812.2 \\ 4375 & 0 \\ 0 & 6250 \\ 2588.8 & 6250 \\ 6250 & 2588.8 \\ 6250 & 0 \\ 0 & 6250 \\ 2588.8 & 6250 \\ 6250 & 2588.8 \\ 6250 & 0 \\ 0 & 8125 \\ 3365.5 & 8125 \\ 8125 & 3365.5 \\ 8125 & 0 \\ 0 & 10\,000 \\ 4142.1 & 10\,000 \\ 10\,000 & 4142.1 \\ 10\,000 & 0 \end{Bmatrix} \quad \mathbf{P}^{e,3} = \begin{Bmatrix} 0 & 250 \\ 690.36 & 2500 \\ 1279.6 & 2255.9 \\ 2255.9 & 1279.6 \\ 2500 & 690.36 \\ 2500 & 0 \\ 0 & 375 \\ 1035.5 & 3750 \\ 1919.4 & 3383.9 \\ 3383.9 & 1919.4 \\ 3750 & 1035.5 \\ 3750 & 0 \\ 0 & 500 \\ 1380.7 & 5000 \\ 2559.2 & 4511.8 \\ 4511.8 & 2559.2 \\ 5000 & 1380.7 \\ 5000 & 0 \\ 0 & 6250 \\ 1725.9 & 6250 \\ 3199.0 & 5639.8 \\ 5639.8 & 3199 \\ 6250 & 1725.9 \\ 6250 & 0 \\ 0 & 6250 \\ 1725.9 & 6250 \\ 3199 & 5639.8 \\ 5639.8 & 3199 \\ 6250 & 1725.9 \\ 6250 & 0 \\ 0 & 7500 \\ 2071.1 & 7500 \\ 3838.8 & 6767.8 \\ 6767.8 & 3838.8 \\ 7500 & 2071.1 \\ 7500 & 0 \\ 0 & 8750 \\ 2416.2 & 8750 \\ 4478.6 & 7895.7 \\ 7895.7 & 4478.6 \\ 8750 & 2416.2 \\ 8750 & 0 \\ 0 & 10\,000 \\ 2761.4 & 10\,000 \\ 5118.4 & 9023.7 \\ 9023.7 & 5118.4 \\ 10\,000 & 2761.4 \\ 10\,000 & 0 \end{Bmatrix}$$

DOI: 10.1002/nme

REFERENCES

1. Griffith AA. The phenomena of rupture and flow in solids. *Philosophical Transactions of the Royal Society of London* 1921; **A221**:163–198.
2. Irwin G. Analysis of stresses and strains near the end of a crack traversing a plate. *Journal of Applied Mechanics* 1957; **24**:361–364.
3. Dugdale DS. Yielding of steel sheets containing slits. *Journal of the Mechanics and Physics of Solids* 1960; **8**: 100–104.
4. Barenblatt GI. The mathematical theory of equilibrium cracks in brittle fracture. *Advances in Applied Mechanics* 1962; **7**:55–129.
5. Rice JR, Simons DA. The stabilization of spreading shear faults by coupled deformation-diffusion effects in fluid-infiltrated porous materials. *Journal of Geophysical Research* 1976; **81**:5322–5334.
6. Terzaghi K. *Theoretical Soil Mechanics*. Wiley & Sons: New York, 1943.
7. Biot MA. *Mechanics of Incremental Deformations* (2nd edn). Wiley & Sons: Chichester, 1998.
8. de Boer R. Highlights in the historical development of the porous media theory: toward a consistent macroscopic theory. *Applied Mechanics Reviews* 1996; **49**:201–262.
9. Lewis RW, Schrefler BA. *The Finite Element Method in the Static and Dynamic Deformation and Consolidation of Porous Media* (Second Edition). Wiley & Sons: Chichester, 1998.
10. Segura JM, Carol I. Coupled HM analysis using zero-thickness interface elements with double nodes. Part I: theoretical model. *International Journal for Numerical and Analytical Methods in Geomechanics* 2008; **32**: 2083–2101.
11. Carrier B, Granet S. Numerical modelling of hydraulic fracture problem in permeable medium using cohesive zone model. *Engineering Fracture Mechanics* 2012; **79**:312–328.
12. Secchi S, Simoni L, Schrefler BA. Mesh adaptation and transfer schemes for discrete fracture propagation in porous materials. *International Journal for Numerical and Analytical Methods in Geomechanics* 2007; **31**:331–345.
13. Boone TJ, Ingraffea AR. A numerical procedure for simulation of hydraulic-driven fracture propagation in poroelastic media. *International Journal for Numerical and Analytical Methods in Geomechanics* 1990; **14**:27–47.
14. de Borst R, Réthoré J, Abellan MA. A numerical approach for arbitrary cracks in a fluid-saturated porous medium. *Archive of Applied Mechanics* 2006; **75**:595–606.
15. Réthoré J, de Borst R, Abellan MA. A two-scale approach for fluid flow in fractured porous media. *International Journal for Numerical Methods in Engineering* 2007; **75**:780–800.
16. Réthoré J, de Borst R, Abellan MA. A discrete model for the dynamic propagation of shear bands in fluid-saturated medium. *International Journal for Numerical and Analytical Methods in Geomechanics* 2007; **31**:347–370.
17. Réthoré J, de Borst R, Abellan MA. A two-scale model for fluid flow in an unsaturated porous medium with cohesive cracks. *Computational Mechanics* 2008; **42**:227–238.
18. Irzal F, Remmers JJC, Huyghe JM, de Borst R. A large deformation formulation for fluid flow in a progressively fracturing porous material. *Computer Methods in Applied Mechanics and Engineering* 2013; **256**:29–37.
19. Belytschko T, Black T. Elastic crack growth in finite elements with minimal remeshing. *International Journal for Numerical Methods in Engineering* 1999; **45**:601–620.
20. de Borst R, Crisfield MA, Remmers JJC, Verhoosel CV. *Non-linear Finite Element Analysis of Solids and Structures* (second). Wiley & Sons: Chichester, 2012.
21. Khoei A. *Extended Finite Element Method: Theory and Applications*. Wiley & Sons: Chichester, 2014.
22. Malakpoor P, Kaasschieter EF, Huyghe JM. Mathematical modelling and numerical solution of swelling cartilaginous tissues. Part II: mixed hybrid finite element solution. *ESAIM: Mathematical Modelling and Numerical Analysis* 2007; **41**:679–712.
23. Kagan P, Fischer A, Bar-Yoseph PZ. New B-spline finite element approach for geometrical design and mechanical analysis. *International Journal for Numerical Methods in Engineering* 1998; **41**:435–458.
24. Kagan P, Fischer A. Integrated mechanically based CAE system using B-spline finite elements. *Computer-Aided Design* 2000; **32**:539–552.
25. Hughes TJR, Cottrell JA, Bazilevs Y. Isogeometric analysis: CAD, finite elements, NURBS, exact geometry and mesh refinement. *Computer Methods in Applied Mechanics and Engineering* 2005; **194**:4135–4195.
26. Cottrell JA, Hughes TJR, Bazilevs Y. *Isogeometric Analysis: Toward Integration of CAD and FEA*. Wiley & Sons: Chichester, 2009.
27. Bazilevs Y, Calo VM, Cottrell JA, Evans JA, Hughes TJR, Lipton S, Scott MA, Sederberg TW. Isogeometric analysis using T-splines. *Computer Methods in Applied Mechanics and Engineering* 2010; **199**:229–263.
28. Scott MA, Borden MJ, Verhoosel CV, Sederberg TW, Hughes TJR. Isogeometric finite element data structures based on Bézier extraction of T-splines. *International Journal for Numerical Methods in Engineering* 2011; **88**:126–156.
29. May S, Vignollet J, de Borst R. The role of the Bézier extraction operator for T-splines of arbitrary degree: linear dependencies, partition of unity property, nesting behaviour and local refinement. *International Journal for Numerical Methods in Engineering* 2015; **103**:547–581.
30. Irzal F, Remmers JJC, Verhoosel CV, de Borst R. Isogeometric finite element analysis of poroelasticity. *International Journal for Numerical and Analytical Methods in Geomechanics* 2013; **37**:1891–1907.
31. Brezzi F, Fortin M. *Mixed and Hybrid Finite Element Methods*. Springer: Berlin, 1991.
32. Chapelle D, Bathe KJ. The inf-sup test. *Computers & Structures* 1993; **47**:537–545.

DOI: 10.1002/nme

33. Sandhu RS, Liu H, Singh KJ. Numerical performance of some finite element schemes for analysis of seepage in porous elastic media. *International Journal for Numerical and Analytical Methods in Geomechanics* 1977; **1**: 177–194.
34. Irzal F, Remmers JJC, Verhoosel CV, de Borst R. An isogeometric analysis Bézier interface element for mechanical and poromechanical fracture problems. *International Journal for Numerical Methods in Engineering* 2014; **97**: 608–628.
35. Vignollet J, May S, de Borst R. On the numerical integration of isogeometric interface elements. *International Journal for Numerical Methods in Engineering* 2015; **102**:1733–1749.
36. Thomas DC, Scott MA, Evans JA, Tew K, Evans EJ. Bézier projection: a unified approach for local projection and quadrature-free refinement and coarsening of NURBS and T-splines with particular application to isogeometric design and analysis. *Computer Methods in Applied Mechanics and Engineering* 2015; **284**:55–105.
37. Vignollet J, Kaczmarczyk L, Pearce CJ. A Galerkin least-square stabilisation technique for hyperelastic biphasic soft tissue. *Computers & Structures* 2013; **118**:109–114.
38. Borden MJ, Scott MA, Evans JA, Hughes TJR. Isogeometric finite element data structures based on Bézier extraction. *International Journal for Numerical Methods in Engineering* 2011; **87**:15–47.
39. D'Angelo C, Scotti A. A mixed finite element method for Darcy flow in fracture porous media with non-matching grids. *ESAIM: Mathematical Modelling and Numerical Analysis* 2012; **46**:465–489.
40. Formaggia L, Fumagalli A, Scotti A, Ruffo P. A reduced model for Darcy's problem in networks of fractures. *ESAIM: Mathematical Modelling and Numerical Analysis* 2014; **48**:1089–1116.
41. Hohberg JM. A note on spurious oscillations in FEM joint elements. *Earthquake Engineering & Structural Dynamics* 1990; **19**:773–779.
42. Schellekens JCJ, de Borst R. On the numerical integration of interface elements. *International Journal for Numerical Methods in Engineering* 1993; **36**:43–66.
43. Piegl L, Tiller W. *The NURBS Book*. Springer: Berlin, 1997.

DOI: 10.1002/nme